 SDHM, vol.13, no.1, pp.41-59, 2019

Multi-Mode Guided Waves Based Reference-Free Damage Diagnostic Imaging in Plates

Jiaqi Zhang[1], Kehai Liu[2,*], Chang Gao[1], Zhanjun Wu[1], Yuebin Zheng[1] and Dongyue Gao[3]

Abstract: Probability-based diagnostic imaging (PDI) is one of the most well-known damage identification methods using guided waves. It is usually applied to diagnose damage in plates. The previous studies were dependent on the certain damage index (DI) which is always calculated from the guided wave signals. In conventional methods, DI is simply defined by comparing the real-time data with the baseline data as reference. However, the baseline signal is easily affected by varying environmental conditions of structures. In this paper, a reference-free diagnostic imaging method is developed to avoid the influence of environmental factors, such as temperature and load conditions. The DI is defined based on the mode conversion of multi-mode guided waves with real-time signals without baseline signals. To improve the accuracy of diagnosis, two terms are included in the reference-free DI. One is called energy DI, which is defined based on the feature of signal energy. The other is called correlation DI and is defined based on the correlation coefficient. Then the PDI algorithm can be carried out instantaneously according to the reference-free DI. The real-time signals which are used to calculate DI are collected by the piezoelectric lead zirconate titanate (PZT) transducers placed on both sides of a plate. The numerical simulations by the finite element (FE) method on aluminum plates with PZT arrays are performed to validate the effectiveness of the reference-free damage diagnostic imaging. The approach is validated by two different arrays: a circle network and a square network. The results of diagnostic imaging are demonstrated and discussed in this paper. Furthermore, the advantage of reference-free DI is investigated by comparing the accuracy of defined reference-free DI and energy DI.

Keywords: Multi-mode guided waves, probability-based diagnostic imaging, reference-free, mode conversion.

[1] State Key Laboratory of Structural Analysis for Industrial Equipment, Dalian University of Technology, Dalian, 116024, China.

[2] School of Civil Engineering, Dalian University of Technology, Dalian, 116024, China.

[3] School of Aeronautics and Astronautics, Sun Yat-sen University, Guangzhou, 510275, China.

[*] Corresponding Author: Kehai Liu. Email: liukh@dlut.edu.cn.

SDHM. Doi: 10.32604/sdhm.2019.05142 www.techscience.com/sdhm

1 Introduction

As important parts of engineering structures, large-area plates usually suffer adverse serving conditions or even sudden impacts, which may cause damage and jeopardize structural reliability and safety. Therefore, the development of nondestructive testing (NDT) and structural health monitoring (SHM) that can diagnose structural damage is imperative. A large body of research has been conducted on structural health monitoring [Chang (1998); Qing, Beard, Kumar et al. (2006); Wu, Qing, Ghosh et al. (2008); Cao, Cheng, Su et al. (2012); Lima, Miller and Doh (2013); Amafabia, Montalvão, David-West et al. (2017); Kong (2018)]. Among them, the guided wave is widely used as one of the most encouraging tools for quantitative identification of damage because of the large volumetric coverage and good sensitivity to damage [Su, Ye and Lu (2006); Cao and Qiao (2008); Li, Murayama, Kageyama et al. (2009); Hu, Cai, Zhu et al. (2012); Gao, Wang, Wu et al. (2013); Ren and Lissenden (2015); Zheng, Liu, Wu et al. (2018)].

Damage diagnostic imaging technology has attracted increasing preference as it yields an intuitional quantitative map concerning the structural health [Wu, Liu, Wang et al. (2014)]. Among the damage diagnostic imaging methods, the probability-based diagnostic imaging (PDI) method using guided waves is increasingly used for their high sensitivity to structural damage in recent years. The PDI method has been studied intensively by many researchers. Zhao et al. proposed a PDI method depending on the correlation analysis and applied it in estimating the location of defects on an aircraft wing [Zhao, Gao, Zhang et al. (2007)]. Koduru et al. improved a PDI algorithm with designed annular array sensors for mode controlling, which showed a remarkable improvement in the ability to distinguish a real corrosion defect from any other water traces on structures [Koduru and Rose (2009)]. Zhou et al. developed a PDI approach using hybrid features extracted from ultrasonic guided waves. This approach was employed to identify some representative damage scenarios in plates [Zhou, Su and Cheng (2011)]. Gao et al. introduced a local PDI imaging method for multi-damage identification, which included a path damage judgment stage, a multi-damage judgment stage and a multi-damage imaging stage [Gao, Wu, Yang et al. (2016)]. Liu et al. improved a PDI algorithm with weight compensation to improve the ability of damage localization, which was used to identify the damage at different locations with different groups of sensing paths on a stiffened composite panel [Liu, Ma, Wu et al. (2016)].

Despite its ability of delivering good performance in damage localization, PDI algorithms usually require baseline data collected at the pristine condition to calculate damage index (DI). In previous research, five different kinds of DIs have been studied. Among them, two kinds were extracted from the scatter signal (SST [Michaels (2008)] and SSS [Monnier (2006)]), two kinds were based on the signal difference (SDT [Qing, Chan, Beard et al. (2006)] and SDS) and the fifth kind, SDCC, was based on the correlation coefficient [Zhao, Gao, Zhang et al. (2007)]. All of them were dependent on baseline data. However, the dependence of DI calculation on the baseline data may lead to false positive indications of damage due to its susceptibility to varying environmental conditions of structures [Kim and Sohn (2006)].

Kim and Sohn developed a new guided wave based method to detect crack damage in a thin metal structure without using prior baseline data. The method was implemented

using a new DI based on mode conversion [Kim and Sohn (2007)]. Mode conversion can occur during the process of guided wave scattering in the case of non-symmetric thickness variation [Cho (2002)]. These studies could identify the presence of damage and the approximate location in the direct path between transducers. Nevertheless, the mode conversion has not been used for damage diagnostic imaging yet.

In this paper, a novel reference-free PDI method on the basis of the mode conversion of multi-mode guided waves is developed to identify damage in plates, which can avoid the environmental influence on diagnostic results. Firstly, the extraction method of modes in a T-shaped stringer is proposed. The pristine modes and converted modes can be extracted from real-time signals. Then, a new reference-free DI with two terms is defined in terms of the extractive modes, which is used in the PDI algorithm for the imaging. Finally, the numerical results show that the method is capable of damage diagnostic imaging in plates.

2 Damage diagnostic imaging approach

2.1 The extraction of converted modes

Mode conversion phenomena of guided waves in plates were found in the past years [Cho and Rose (1996)]. Mode conversion occurs due to the non-symmetric thickness variation and damage in plates almost belongs to non-symmetric thickness variation [Cho (2002)]. Therefore, if guided waves propagating along a plate encounter a sudden thickness discontinuity such as cracks or corrosion, some modes would convert to other modes. Some mode conversion phenomena in damaged plates are shown in Fig. 1. Even same mode can be divided into two different types according to the deformed shapes of the surface of plates. The mode, whether S_0 or A_0, can only convert to the mode with the same deformed shapes.

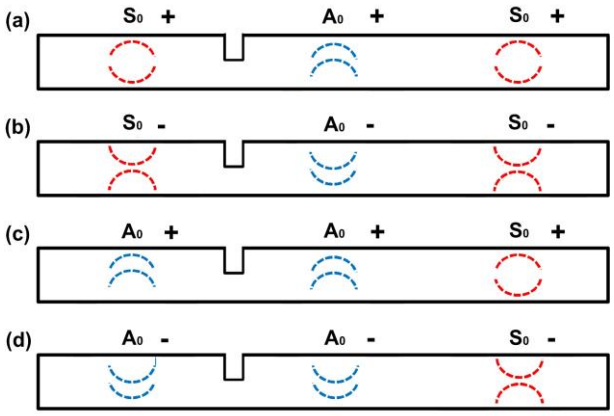

Figure 1: The mode conversion phenomena in damaged plates

The additional modes are named M_1 and M_2 form due to the crack and signals M_1 and M_2 are both between signals S_0 and A_0. Note that M_1 and M_2 could be either the converted S_0

or A_0 according to the relative position of the crack and the actuating and sensing transducers [Kim and Sohn (2007)]. In the previous study, it has been demonstrated that M_1 and M_2 can be extracted from the signals AC, AD, BC and BC which are shown in Fig. 2 [Lee, Kim and Sohn (2008)].

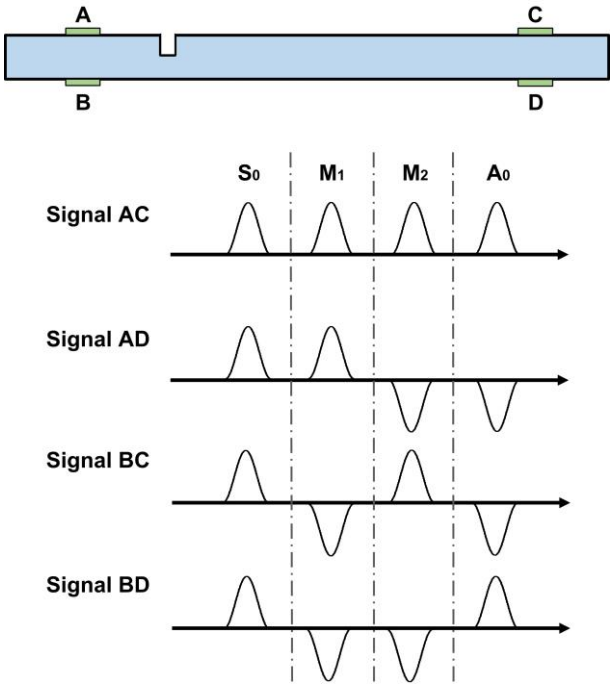

Figure 2: The phases of modes in signals

It is observed that the signals AC, AD, BC and BC are all drawn as the superpositions of signals S_0, A_0, M_1 and M_2. Reversely, the signals S_0, A_0, M_1 and M_2 can be isolated by additions and subtractions of signals AC, AD, BC and BC, which are expressed in matrixes

$$\begin{bmatrix} S_0 \\ M_1 \\ M_2 \\ A_0 \end{bmatrix} = \begin{bmatrix} 1 & 1 & 1 & 1 \\ 1 & 1 & -1 & -1 \\ 1 & -1 & 1 & -1 \\ 1 & -1 & -1 & 1 \end{bmatrix} \times \begin{bmatrix} AB \\ AC \\ DB \\ DC \end{bmatrix} \tag{1}$$

2.2 Reference-free DI calculation

In this study, the DI consists of two terms. The first term of DI is energy DI. It is defined based on the the feature of signal energy which is calculated as

$$ENG = \sqrt{\int_{t_1}^{t_2} s^2(t)dt} \tag{2}$$

where $s(t)$ is the guided wave signal, t_1 and t_2 are the time windows. The time windows in this paper are shown in Fig. 3 where T_S and T_A are the peak times of of the S_0 and A_0 modes. Thus the damage index associated with signal energy is given by

$$DI_{ENG} = ENG_{M_1-M_2} \tag{3}$$

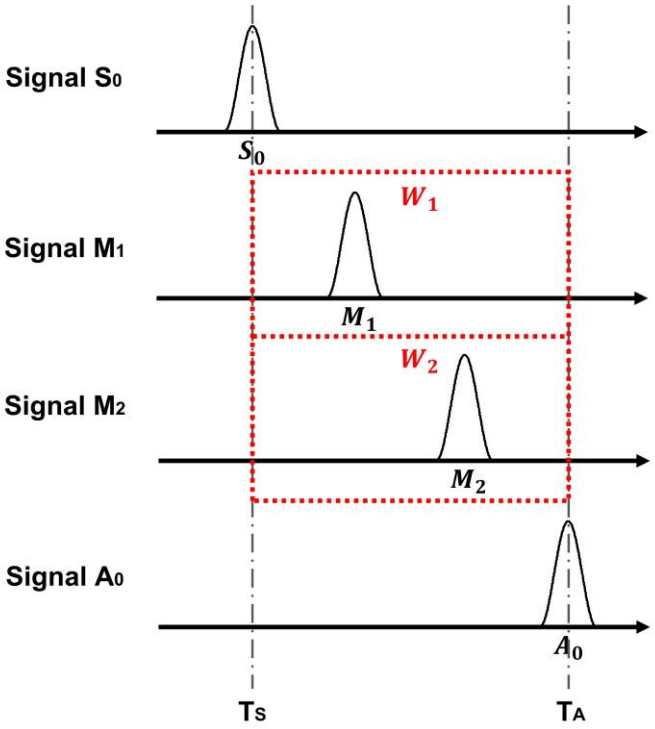

Figure 3: The modes in different time windows

The second term of DI is correlation DI. It is defined based on the correlation coefficient, which has been broadly applied in previous research Zhao et al. [Zhao, Gao, Zhang et al. (2007)]. A correlation coefficient ρ of two signals can be define in a simple mathematical formula. The second term is given by

$$DI_{COR} = 1 - \rho_{M_1M_2} \tag{4}$$

where $\rho_{M_1M_2}$ is the correlation coefficient of signals M_1 and M_2. Finally, the DI in this paper is defined as

$$DI = DI_{ENG} \cdot DI_{COR} \tag{5}$$

2.3 PDI algorithm

In PDI approaches, the monitoring area of a structure is meshed into grids and projected to an image, which concerns the probability of presence of damage. The probability of damage occurring at each grid is yielded with appropriate features extracted from guided wave signals and the probability at certain grid (x, y) can be calculated as

$$P(x, y) = \sum_{i=1}^{N} DI_i \cdot W_i\left[R_i(x, y)\right] \tag{6}$$

where DI_i and $W_i\left[R_i(x, y)\right]$ are respectively the DI and the weight distribution function of the *i*th sensing path. The DI can be calculated by the approach in the last section, and the weight distribution function is the non-negative linear decreasing function which can be written as

$$W_i\left[R_i(x, y)\right] = \begin{cases} 1 - \dfrac{R_i(x, y)}{\beta}, & R_i(x, y) < \beta \\ 0, & R_i(x, y) \geq \beta \end{cases} \tag{7}$$

This weight value increases with a decrease in the relative distance between grid (x, y) and the direct sensing path in which damage can cause the most significant signal change [Zhao, Gao, Zhang et al. (2007)]. $W_i\left[R_i(x, y)\right]$ is dependent on parameter $R_i(x, y)$ which is the relative distance between grid (x, y) and the *i*th sensing path [Wang, Ye, Su et al. (2010)]. $R_i(x, y)$ is expressed as

$$R_i(x, y) = \frac{D_{a,i}(x, y) + D_{s,i}(x, y)}{D_i} - 1 \tag{8}$$

where D_i is the distance between the actuator and sensor of the *i*th sensing path, while $D_{a,i}(x, y)$ and $D_{s,i}(x, y)$ are the distances between grid (x, y) and the actuator and the sensor, respectively, for the *i*th sensing path, as shown in Fig. 4.

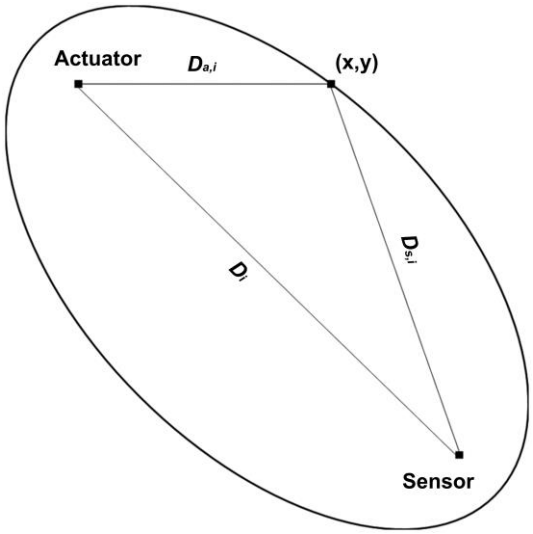

Figure 4: The illustration of relative distance

2.4 Sensing path configurations

Reference-free diagnostic imaging approach is validated by two different groups of sensing paths: a circle network and a square network. The configurations of sensing paths are illustrated in Fig. 5. In this configuration (a), the radius of the transducer array is 200 mm and the transducers' number is 12 on one face. In this configuration (b), the side length of transducer array is 200 mm and the transducers' number is 20 on one face. The other parameters including the monitoring area and the selected paths' number are shown in Tab. 1. Some paths in the configuration (a) are ignored due to the shorter propagation distances which are insufficient to distinguish the modes, and some in the configuration (b) are not used because of overlapping coverage. The selected paths are showed in Tab. 2.

Table 1: Details of two configurations of sensing paths

Network	Sensors number	Paths number	Monitoring area (cm^2)	Minimum path (cm)
Circle	12	30	1256.6	34.64
Square	20	26	1600	40

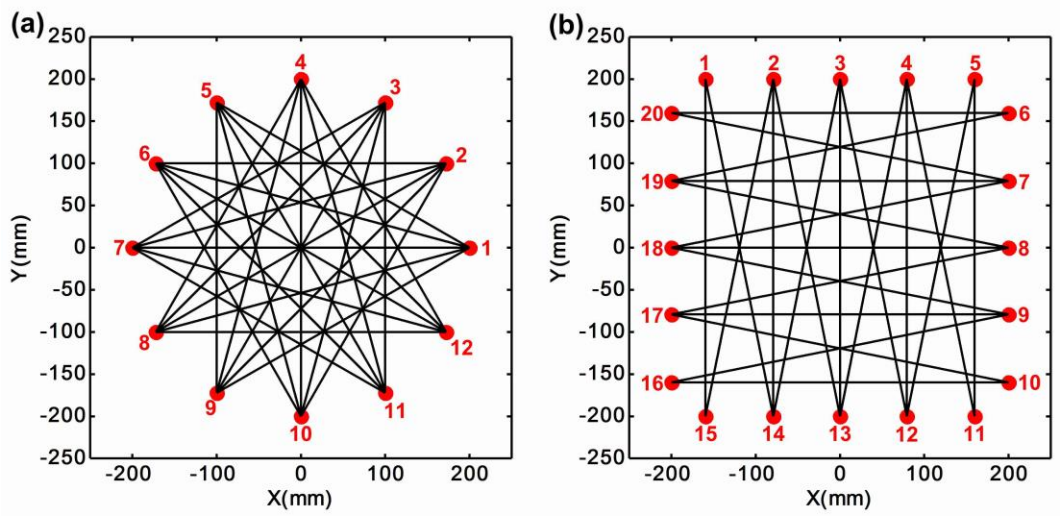

Figure 5: Diagram of the configuration of s transducers paths: (a) circle network; (b) square network

Table 2: Dual PZTs setting of paths

Circle network				Square network			
Path	Dual PZTs	Path	Dual PZTs	Path	Dual PZTs	Path	Dual PZTs
1	1-5	16	4-8	1	1-15	16	7-20
2	1-6	17	4-9	2	1-16	17	7-19
3	1-7	18	4-10	3	2-15	18	7-18
4	1-8	19	4-11	4	2-14	19	8-19
5	1-9	20	4-12	5	2-13	20	8-18
6	2-6	21	5-9	6	3-14	21	8-17
7	2-7	22	5-10	7	3-13	22	9-18
8	2-8	23	5-11	8	3-12	23	9-17
9	2-9	24	5-12	9	4-13	24	9-16
10	2-10	25	6-10	10	4-12	25	10-17
11	3-7	26	6-11	11	4-11	26	10-16
12	3-8	27	6-12	12	5-12		
13	3-9	28	7-11	13	5-11		
14	3-10	29	7-12	14	6-20		
15	3-11	30	8-12	15	6-19		

3 Numerical simulations

3.1 FE modeling

The commercial finite element program ABAQUS/IMPLICIT is used to simulate the reference-free PDI algorithm. An aluminum plate with PZT transducers as the simulation object is modeled in this work. The size of the aluminum plate is 450 mm×450 mm×3 mm and the dimensions of PZT transducers are 8 mm in diameter and 0.2 mm in thickness. The material properties of the aluminum plate are illustrated as follows: mass density of aluminum is 2700 kg/m^3, Young's modulus is 71 GPa and Poisson' ratio is 0.33. The material properties of PZT are illustrated in Tab. 3. To reduce the reflection from boundary, the absorbing region is set up by absorbing layers with incremental damping [Moreau and Castaings (2008)] as shown Fig. 6.

The plate is discretized by C3D6 elements, the absorbing region is discretized by C3D8R elements and the PZT transducers are discretized by C3D8E elements. Some works were investigated to discuss the effect of the element number per wavelength on FE calculation result [Zhang, Zou and Madenga (2006)]. The element size of the plate depends on the minimum wavelength and usually 20 nodes are taken in a minimum wavelength [Li, Jing and Jin (2017)]. The size of the elements used to the plate is 1.5 mm and the size of the elements used to the PZT transducers was 1 mm in order to ensure that a sufficient number of nodes in one transducer were available for collecting signals.

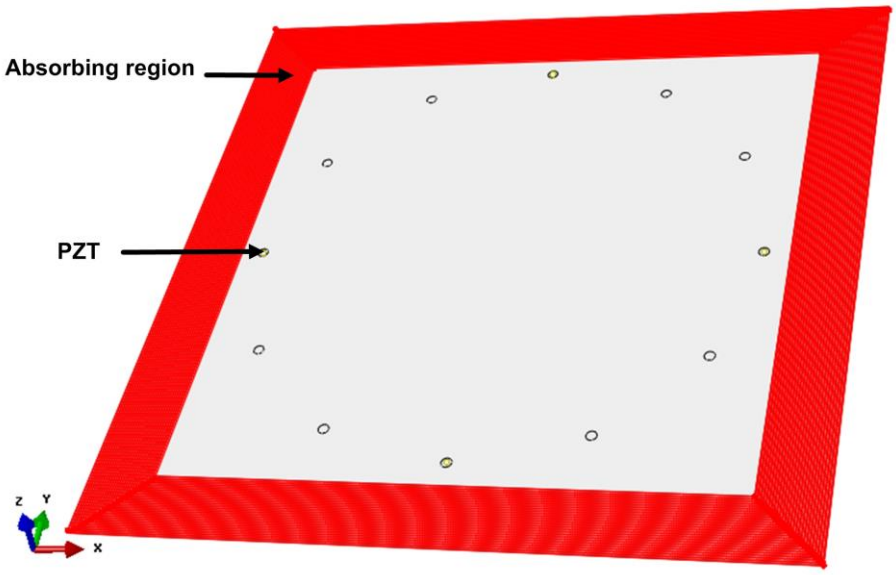

Figure 6: FE model of an aluminum plate with PZT transducers and absorbing region

Table 3: The material properties of PZT

Density (kg/m^3)	Young's modulus (Gpa)	Poisson's ratio	Electrical permittivity (Farad/m)			Piezoelectric (N/Volt • m)
7650	80	0.33	D11 1.0005e-8	D22 1.0005e-8	D33 8.09256e-9	-3.09

A 5 cycle Hanning windowed sinusoidal signal of which the central frequency is 200 kHz is used as the input signal in this paper. The propagation velocity used in this simulation is determined by the dispersion curves of the aluminum plate with the thickness of 3 mm in Fig. 7. It is observed that the mode S_0 and mode A_0 can be excited at 200 kHz without other modes.

Two types of damage are set on the aluminum plates individually as illustrated in Fig. 8. They are both nonpenetrating, which are belong to non-symmetric thickness variation. The size of the square damage is 20 mm×20 mm×2 mm, and the size of the circle damage is φ20 mm×2 mm. The reference-free damage diagnostic imaging of the two plates is carried out individually using the process above.

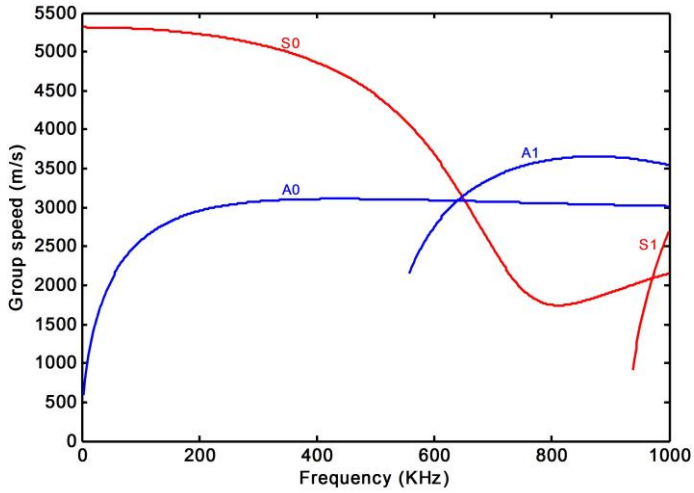

Figure 7: The group velocity dispersion curves of a 3 mm thick aluminum plate

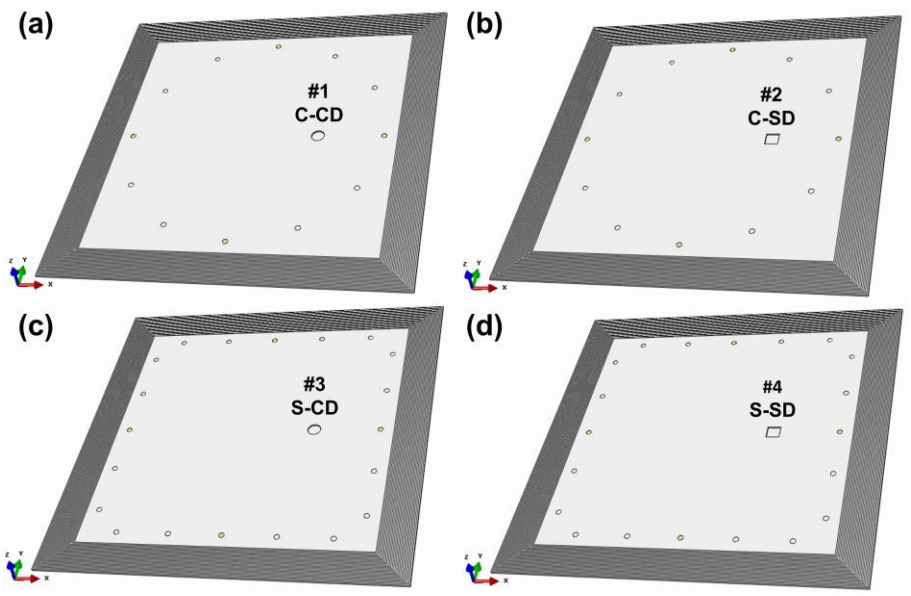

Figure 8: Damage in plates with different path configurations: (a) circle damage in circle network (C-CD); (b) square damage in circle network (C-SD); (c) circle damage in square network (S-SD); (b) square damage in square network (S-SD)

3.2 Results and discussion

Fig. 9 shows the static displacement nephograms of different models. It is observed that guided waves convert to new modes after encountering damage because the nonpenetrating damage belongs to the non-symmetric thickness variation along the direction of guided wave propagation. The signals with individual mode can be isolated from the response signals by Eq. (1), and the results are shown in Fig. 10.

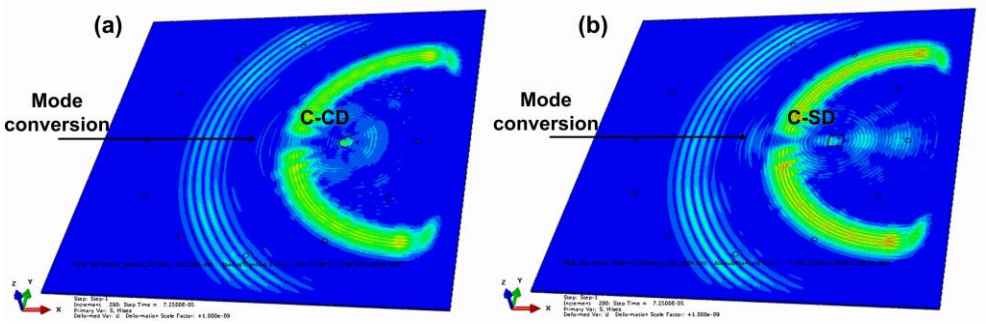

Figure 9: Static images of FE models with different types of damage: (a) circle damage; (b) square damage

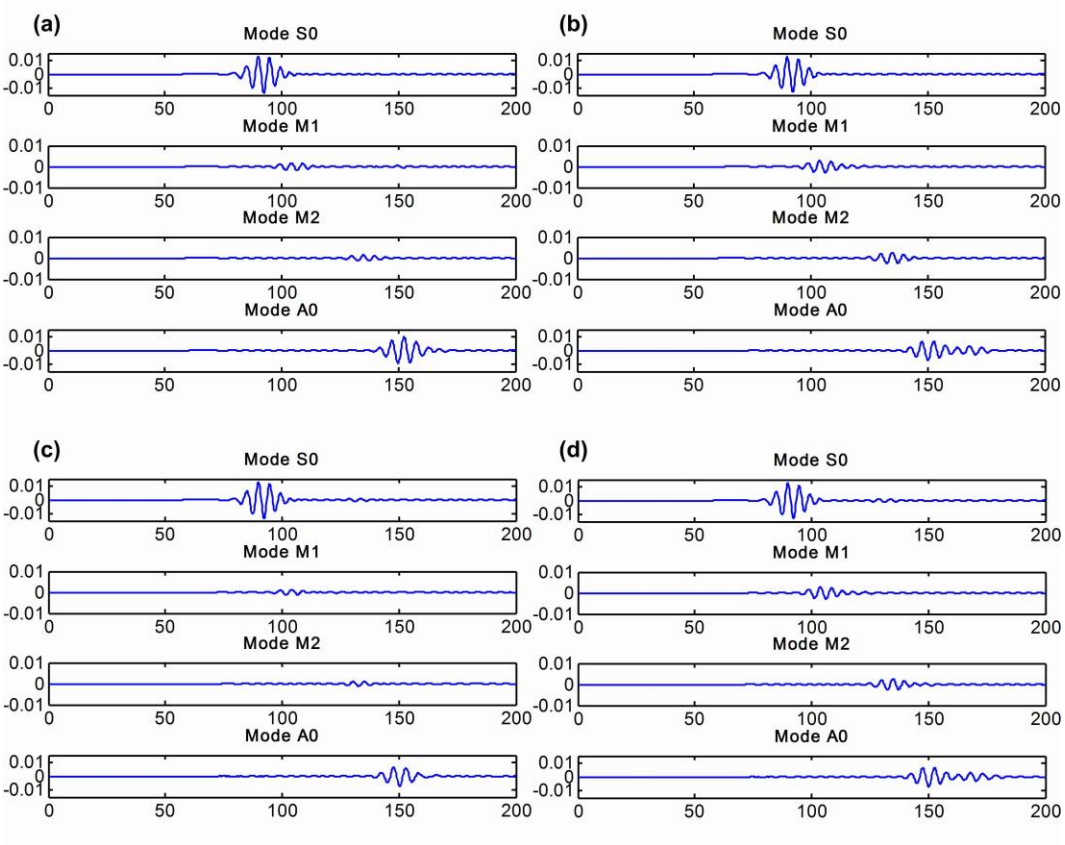

Figure 10: Signals of guided wave in direct path: (a) C-CD; (b) C-SD; (b) S-CD; (b) S-SD

The reference-free DI of all damage types calculated from the isolated signals are illustrated in Fig. 11 and Fig. 12 in which the energy DI and combinational DI are both shown for the comparison. And the comparison of the energy DI and combinational DI indicates that the combinational DI can reduce the impact of non-damaged sensing paths. Therefore the combinational DI can improve the precision of diagnosis.

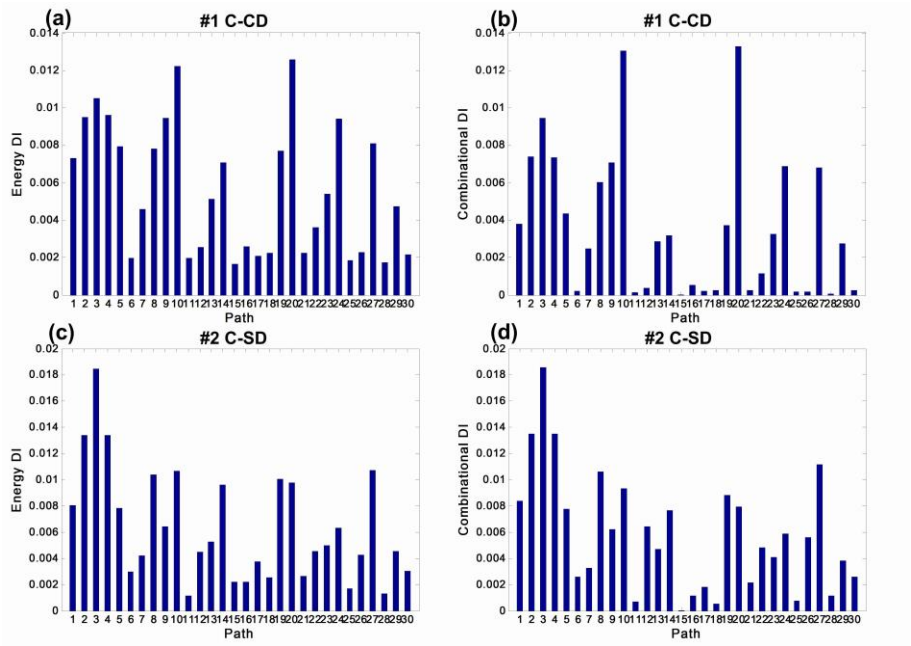

Figure 11: Reference-free DI of each paths from circle network: (a) energy DI of C-CD; (b) combinational DI of C-CD; (c) energy DI of C-SD; (d) combinational DI of C-SD

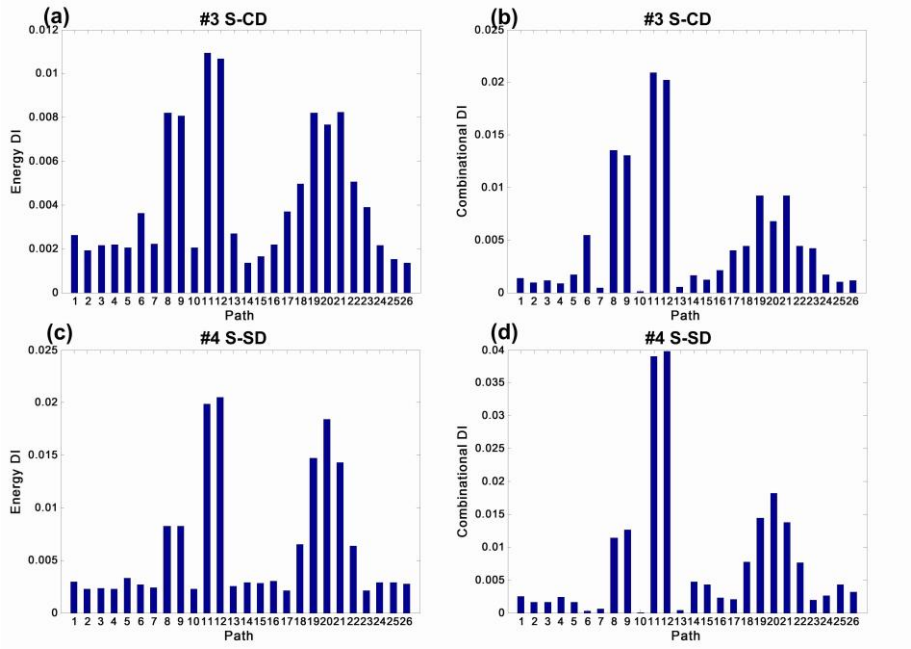

Figure 12: Reference-free DI of each paths from square network: (a) energy DI of S-CD; (b) combinational DI of S-CD; (c) energy DI of S-SD; (d) combinational DI of S-SD

The results of the PDI calculated on the basis of the DIs are shown in Fig. 13 and Fig. 14 for circle and square networks respectively. Fig. 13(a) and Fig. 13(c) are the diagnostic images only using energy DI, and Fig. 13(b) and Fig. 13(d) using combinational DI. Correspondingly Fig. 14 is same as Fig. 13.

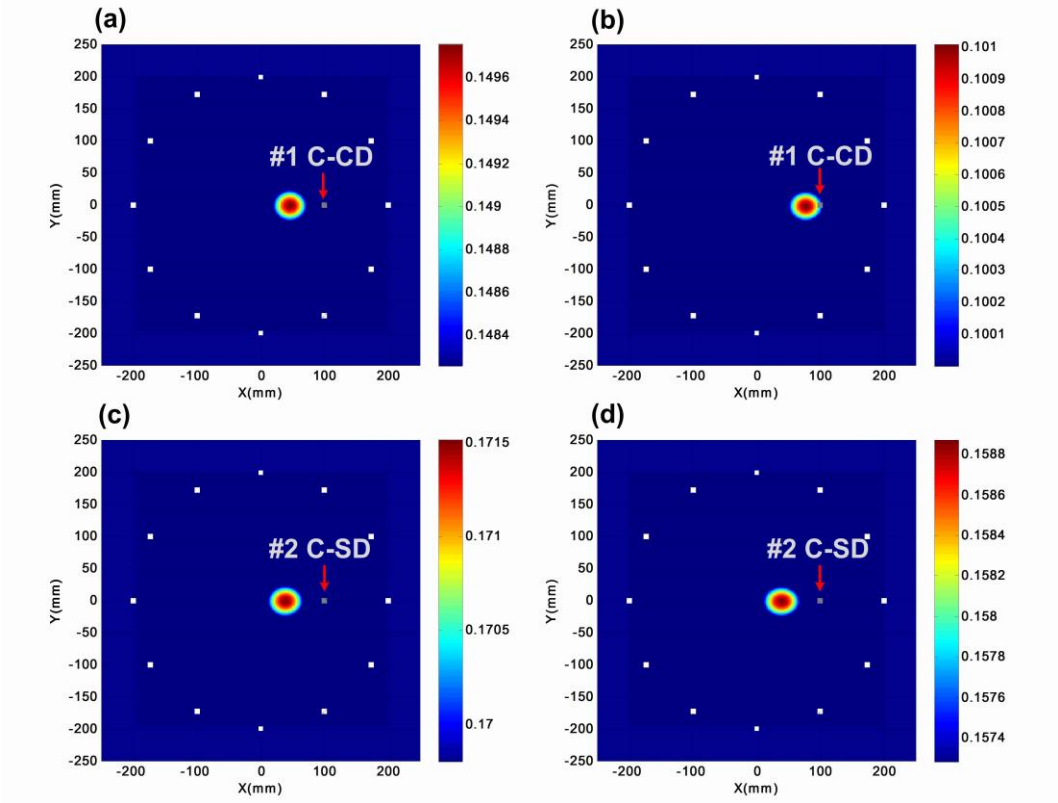

Figure 13: Diagnostic images of PDI algorithm from circle network: (a) C-CD image using energy DI; (b) C-CD image using combinational DI; (c) C-SD image using energy DI; (d) C-SD image using combinational DI

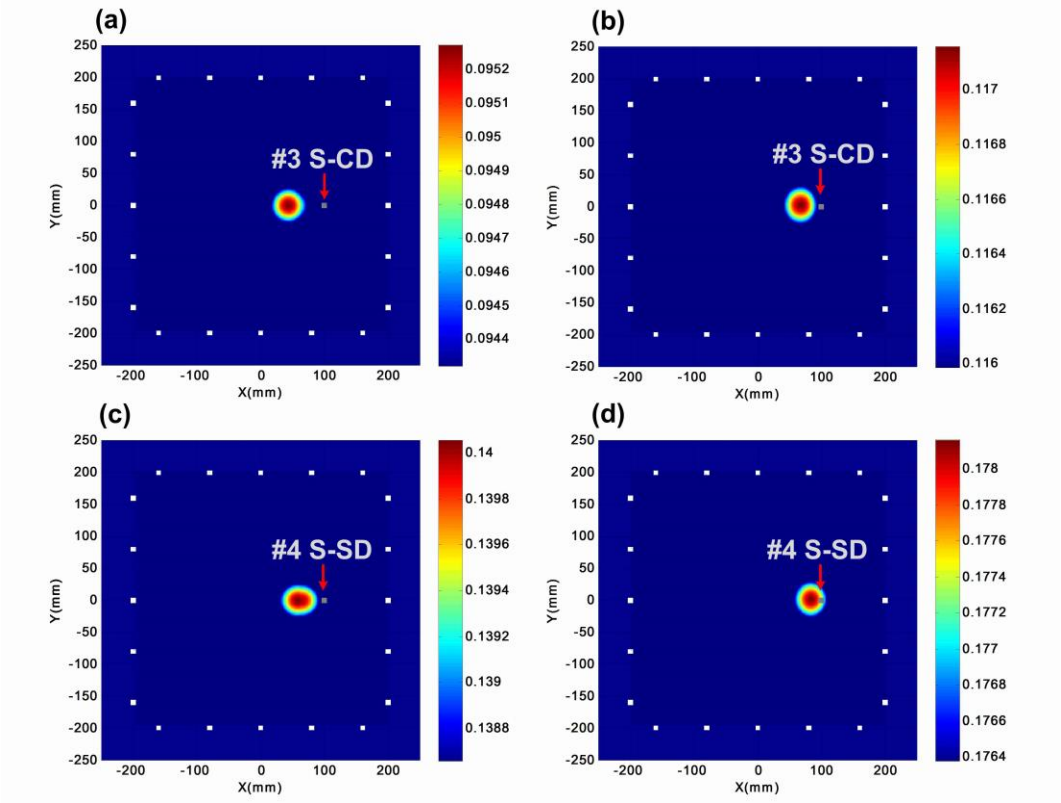

Figure 14: Diagnostic images of PDI algorithm from square network: (a) S-CD image using energy DI; (b) S-CD image using combinational DI; (c) S-SD image using energy DI; (d) S-SD image using combinational DI

Tab. 4 lists the damage monitoring errors of circle network and square network, respectively, among which damage absolute localization errors are the distance between the peak points of the individual images and actual locations of damage. Here, a relative localization error is given by

$$E_{relative} = \frac{N_{PZT} N_{path}}{S_{monitor} L_{\min path}} \times E_{absolute} \times 100\% \tag{9}$$

where $E_{absolute}$ is the absolute error, N_{PZT} is the number of PZT transducers, N_{path} is the number of paths, $S_{monitor}$ is the monitoring area and $L_{\min path}$ is the length of the minimum path.

Table 4: The localization errors of damage

	Energy DI		Combinational DI	
Damage	Absolute error	Relative error	Absolute error	Relative error
#1 C-CD	5.5 cm	4.55%	2.3 cm	1.91%
#2 C-SD	6.1 cm	5.05%	6.1 cm	5.05%
#3 S-CD	5.7 cm	4.63%	3.3 cm	2.68%
#4 S-SD	4.3 cm	3.49%	1.7 cm	1.38%

Fig. 15 shows the comparison of relative localization errors calculated from the two different DI. It is observed that the combinational DI obtains more accurate localization than the conventional energy DI.

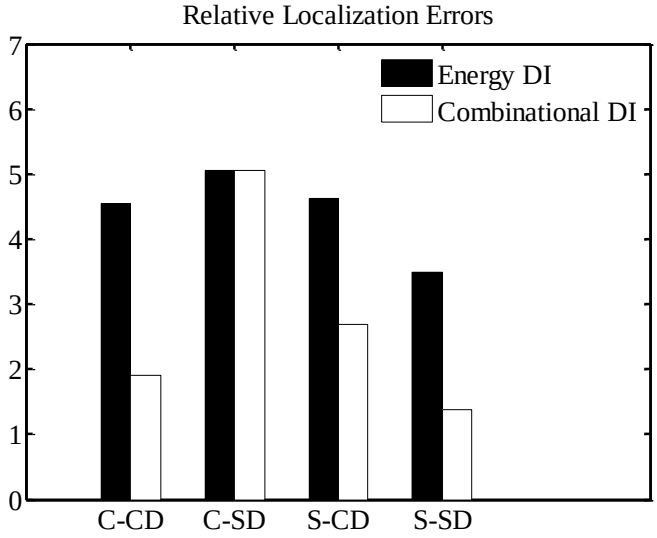

Figure 15: The relative localization errors of reference-free PDI in numerical simulations

4 Conclusion

This paper has presented a novel reference-free damage diagnostic imaging method based on the probability-based diagnostic imaging (PDI) without baseline data vulnerable to the labile environment. The reference-free PDI algorithm in this paper is on the basis of the damage index (DI) like the previous PDI algorithms. However, the DI is defined by the converted modes extracted from real-time multi-mode guided wave signals. Thus the

dependence on the baseline data is eliminated on the strength of mode conversion. Futhermore, the reference-free DI consists of two terms in order to improve the accuracy of diagnosis. They are the energy DI defined based on the feature of signal energy and the correlation DI defined based on the correlation coefficient. By applying the reference-free DI to the PDI algorithm, diagnostic images of two different configurations, circle network and square network, are clear and accurate. The effectiveness of this method is assessed over the numerical simulations by the FE method. Noted that with the combinational DI adopted instead of the energy DI, higher localization accuracy is obtained. More tests at low-temperature environment need to be carried out experimentally to further prove the effectiveness of the proposed method without baseline data.

Acknowledgement: This work was supported by the National Key Research and Development Program of China (Grant No. 2016YFF0203002), the National Natural Science Foundation of China (Grant No. 11702051), China Post-doctoral Science Foundation (Grant No. 2017M610176) and the Fundamental Research Funds for the Central Universities (DUT16ZD214).

Declaration of conflicting interests: The authors declared no potential conflicts of interest with respect to the research, authorship, and/or publication of this article.

References

Amafabia, D. M.; Montalvão, D.; David-West, O.; Haritos, G. (2017): A review of structural health monitoring techniques as applied to composite structures. *Structural Durability and Health Monitoring*, vol. 11, no. 2, pp. 91-147.

Cao, M.; Cheng, L.; Su, Z.; Xu, H. (2012): A multi-scale pseudo-force model in wavelet domain for identification of damage in structural components. *Mechanical Systems and Signal Processing*, vol. 28, pp. 638-659.

Cao, M.; Qiao, P. (2008): Damage detection of laminated composite beams with progressive wavelet transforms. *Nondestructive Characterization for Composite Materials, Aerospace Engineering, Civil Infrastructure, and Homeland Security 2008-International Society for Optics and Photonics*, vol. 6934, 693402.

Chang, F. K. (1998): *Structural Health Monitoring: Current Status and Perspectives*. Crc Press, Boca Raton.

Cho, Y. (2002): Estimation of ultrasonic guided wave mode conversion in a plate with thickness variation. *IEEE Transactions on Ultrasonics, Ferroelectrics, and Frequency Control*, vol. 47, no. 3, pp. 591-603.

Cho, Y.; Rose, J. L. (1996): A boundary element solution for a mode conversion study on the edge reflection of lamb waves. *Journal of the Acoustical Society of America*, vol. 99, no. 4, pp. 2097.

Gao, D.; Wang, Y.; Wu, Z.; Gorgin, R. (2013): Damage extension diagnosis method for typical structures of composite aircraft based on lamb waves. *Structural Durability and Health Monitoring*, vol. 9, no. 3, pp. 233-252.

Gao, D.; Wu, Z.; Yang, L.; Zheng, Y. (2016): Guide waves-based multi-damage identification using a local probability-based diagnostic imaging method. *Smart Materials and Structures*, vol. 25, no. 4, 045009.

Hu, N.; Cai, Y.; Zhu, G.; Tsuji, C.; Liu, Y. et al. (2012): Characterization of damage size in metallic plates using Lamb waves. *Structural Health Monitoring*, vol. 11, no. 2, pp. 125-137.

Kim, S. B.; Sohn, H. (2006): Application of time-reversal guided waves to field bridge testing for baseline-free damage diagnosis. *Proceedings of the SPIE-Health Monitoring and Smart Nondestructive Evaluation of Structural and Biological Systems V*, vol. 6177, 617706.

Kim, S. B.; Sohn, H. (2007): Instantaneous reference-free crack detection based on polarization characteristics of piezoelectric materials. *Smart Materials and Structures*, vol. 16, no. 6, pp. 2375-2387.

Koduru, J. P.; Rose, J. L. (2009): Guided wave annular array sensor design for improved tomographic imaging. *Thompson DO and Chimenti DE (eds)-Review of Progress in Quantitative Nondestructive Evaluation*, vol. 28, pp. 658-665.

Kong, F. T. (2018): Time series analysis for vibration-based structural health monitoring: a review. *Structural Durability and Health Monitoring*, vol. 12, no. 3, pp. 129-147.

Lee, C.; Kim, S.; Sohn, H. (2008): The effect of through-the-thickness holes on a reference-free damage diagnosis technique. *Proceedings of SPIE-The International Society for Optical Engineering*, vol. 6932, 69321U.

Li, D.; Jing, Z.; Jin, M. (2017): Plate-like structure damage location identification based on Lamb wave baseline-free probability imaging method. *Advances in Mechanical Engineering*, vol. 9, no. 1, pp. 1-10.

Li, F.; Murayama, H.; Kageyama, K.; Shirai, T. (2009): Guided wave and damage detection in composite laminates using different fiber optic sensors. *Sensors*, vol. 9, no. 5, pp. 4005-4021.

Lima, M. M.; Miller, D.; Doh, J. H. (2013): Structural health monitoring of concrete bridges in guilan province based on a visual inspection method. *Structural Durability and Health Monitoring*, vol. 9, no. 4, pp. 269-285.

Liu, K.; Ma, S.; Wu, Z.; Zheng, Y.; Qu, X. et al. (2016): A novel probability-based diagnostic imaging with weight compensation for damage localization using guided waves. *Structural Health Monitoring*, vol. 15, no. 2.

Michaels, J. E. (2008): Detection, localization and characterization of damage in plates with an *in situ* array of spatially distributed ultrasonic sensors. *Smart Materials and Structures*, vol. 17, no. 3, 035035.

Monnier, T. (2006): Lamb waves-based impact damage monitoring of a stiffened aircraft panel using piezoelectric transducers. *Journal of Intelligent Material Systems and Structures*, vol. 17, no. 5, pp. 411-421.

Moreau, L.; Castaings, M. (2008): The use of an orthogonality relation for reducing the size of finite element models for 3D guided waves scattering problems. *Ultrasonics*, vol. 48, no. 5, pp. 357-366.

Qing, X. P.; Beard, S. J.; Kumar, A.; Hannum, R. (2006): A real-time active smart patch system for monitoring the integrity of bonded repair on an aircraft structure. *Smart Materials and Structures*, vol. 15, no. 3, N66.

Qing, X. P.; Chan, H.; Beard, S. J.; Kumar, A. (2006): An active diagnostic system for structural health monitoring of rocket engines. *Journal of Intelligent Material Systems and Structures*, vol. 17, no. 7, pp. 619-628.

Ren, B.; Lissenden, C. J. (2015): Phased array transducers for ultrasonic guided wave mode control and identification for aircraft structural health monitoring. *Materials Evaluation*, vol. 73, no. 8.

Su, Z.; Ye, L.; Lu, Y. (2006): Guided Lamb waves for identification of damage in composite structures: a review. *Journal of Sound and Vibration*, vol. 295, no. 3, pp. 753-780.

Wang, D.; Ye, L.; Su, Z.; Lu, Y.; Li, F. et al. (2010): Probabilistic damage identification based on correlation analysis using guided wave signals in aluminum plates. *Structural Health Monitoring*, vol. 9, no. 2, pp. 133-144.

Wu, Z.; Liu, K.; Wang, Y.; Zheng, Y. (2015): Validation and evaluation of damage identification using probability-based diagnostic imaging on a stiffened composite panel. *Journal of Intelligent Material Systems and Structures*, vol. 26, no. 16, pp. 2181-2195.

Wu, Z.; Qing, X. P.; Ghosh, K.; Karbhar, V.; Chang, F. K. (2008): Health monitoring of bonded composite repair in bridge rehabilitation. *Smart Materials and Structures*, vol. 17, no. 4, 045014.

Zhang, C. S.; Zou, D. H.; Madenga, V. (2006): Numerical simulation of wave propagation in grouted rock bolts and the effects of mesh density and wave frequency. *International Journal of Rock Mechanics and Mining Sciences*, vol. 43, no. 4, pp. 634-639.

Zhao, X.; Gao, H.; Zhang, G.; Ayhan, B.; Yan, F. et al. (2007): Active health monitoring of an aircraft wing with embedded piezoelectric sensor/actuator network: I. defect detection, localization and growth monitoring. *Smart Materials and Structures*, vol. 16, no. 4, pp. 1208.

Zheng, Y.; Liu, K.; Wu, Z.; Gao, D.; Gorgin, R. et al. (2019): Lamb waves and electro-mechanical impedance based damage detection using a mobile PZT transducer set. *Ultrasonics*, vol. 92, pp. 13-20.

Zhou, C.; Su, Z.; Cheng, L. (2011): Probability-based diagnostic imaging using hybrid features extracted from ultrasonic lamb wave signals. *Smart Materials and Structures*, vol. 20, no. 12, 125005.